

# VISION-MAE: A Foundation Model for Medical Image Segmentation and Classification

<sup>1</sup>Zelong Liu, <sup>1</sup>Andrew Tieu, <sup>1</sup>Nikhil Patel, <sup>1</sup>Alexander Zhou, <sup>1</sup>George Soultanidis, <sup>1,2</sup>Zahi A. Fayad, <sup>3,4</sup>Timothy Deyer, <sup>1,2</sup>Xueyan Mei

<sup>1</sup>BioMedical Engineering and Imaging Institute, Icahn School of Medicine at Mount Sinai, New York, NY

<sup>2</sup>Department of Diagnostic, Molecular, and Interventional Radiology, Icahn School of Medicine at Mount Sinai, New York, NY

<sup>3</sup>East River Medical Imaging, New York, NY

<sup>4</sup>Department of Radiology, Cornell Medicine, New York, NY

## Abstract

Artificial Intelligence (AI) has the potential to revolutionize diagnosis and segmentation in medical imaging. However, development and clinical implementation face multiple challenges including limited data availability, lack of generalizability, and the necessity to incorporate multi-modal data effectively. A foundation model, which is a large-scale pre-trained AI model, offers a versatile base that can be adapted to a variety of specific tasks and contexts. Here, we present a novel foundation model, VISION-MAE, specifically designed for medical imaging. Specifically, VISION-MAE is trained on a dataset of 2.5 million unlabeled images from various modalities (CT, MR, PET, X-rays, and ultrasound), using self-supervised learning techniques. It is then adapted to classification and segmentation tasks using explicit labels. VISION-MAE has high label efficiency, outperforming several benchmark models in both in-domain and out-of-domain applications, and achieves high performance even with reduced availability of labeled data. This model represents a significant advancement in medical imaging AI, offering a generalizable and robust solution for improving segmentation and classification tasks while reducing the data annotation workload.

## Introduction

Recent advances in the field of artificial intelligence (AI) have given rise to the development of foundation models, machine learning models that are trained on large, diverse datasets that can be adapted to a wide variety of downstream tasks<sup>1</sup>. While traditional deep learning models are specifically trained for designated applications, such as classification of interstitial lung disease<sup>2</sup> or COVID-19<sup>3</sup>, and consistently underperform when repurposed for other tasks<sup>4</sup>, foundation models offer more generalized and adaptable capabilities. Following initial training, foundation models are able to be fine-tuned to a number of different tasks. In the field of medical imaging, foundation models have a wide range of potential applications such as improved diagnostic accuracy, increased efficiency of reads, and prediction of disease outcomes. The incorporation of foundation models into clinical workflows has the potential to revolutionize the field of healthcare delivery.

The Segment Anything Model (SAM)<sup>5</sup>, a foundation model trained on a dataset of 11 million natural images with over 1 billion image masks, showcased the ability to automatically segment any image through the use of prompts. Soon after, this capability was applied to medical images with the release of MedSAM<sup>6</sup>, trained on a large-scale medical imaging dataset with over 1

million medical image-mask pairs across a wide array of modalities and protocols, thus opening the door to many possibilities in the field of medical imaging analysis. In the months since MedSAM's release, increasing numbers of medical imaging foundation models have been reported for a variety of applications. RETFound<sup>7</sup>, a foundation model trained on 1.3 million retina images, offers generalizable capabilities to detect multiple retinal diseases. Other medical foundation models are able to perform segmentation of moving structures<sup>8</sup>, volumetric segmentation<sup>9</sup>, diagnosis and prognosis of ocular disease<sup>10,11</sup>, and assessment of clinical pathology images<sup>12</sup>. Despite these advances, there remain several challenges in the development of foundation models. In addition, the training of foundation models through traditional supervised learning approaches is limited by the need for large quantities of labeled data, which is often a prohibitively time-consuming and cost-intensive process<sup>13</sup>. This is further compounded by an overall lack of high-quality and open-source medical imaging data<sup>14-16</sup>, hindering the generalizability and accuracy of developed models<sup>17,18</sup>.

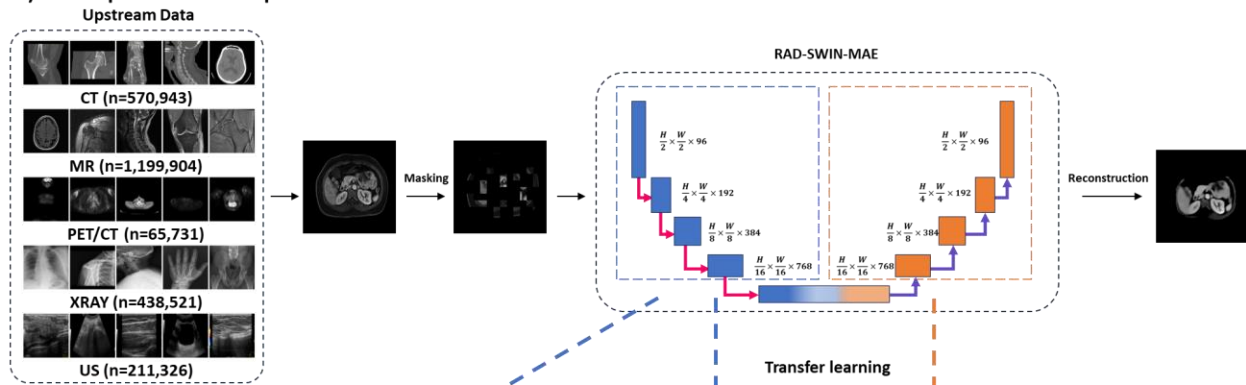
In response to these challenges, current approaches to medical imaging analysis have adopted the use of self-supervised learning (SSL), a training method in which models are instead able to infer labels through latent features of unlabeled data. SSL methods such as SimCLR<sup>19</sup> and Masked Autoencoder<sup>20</sup> have been shown to achieve comparable results or even outperform models using supervised learning methods. Recently, Swin MAE<sup>21</sup>, a masked autoencoder using Swin Transformer as its backbone, demonstrated the feasibility of achieving such results on smaller datasets without the use of pre-trained models.

Given the potential of medical imaging foundation models alongside recent advances in SSL, we propose the VISION-MAE foundation model, a model utilizing a Swin Transformer-based masked autoencoder that can be used for a large variety of downstream tasks. Our model is trained on a dataset composed of 2.5 million clinical images in modalities including CT, MRI, PET/CT, radiography (X-ray), and ultrasound (US). We have applied VISION-MAE to a range of complex segmentation and classification tasks, refining its performance through fine-tuning with specific task labels. Our evaluation process begins with the segmentation of nine diverse tasks, encompassing various imaging modalities, anatomical structures, and multiple diseases. These tasks include the segmentation of abdominal organs in CT and MRI, cardiac structures in MRI, breast and thyroid regions in ultrasound, MRI of the prostate, as well as the segmentation of stroke-affected areas, gliomas, and skin lesions. Additionally, we assess VISION-MAE in five distinct classification tasks. These involve the diagnosis of COVID-19, the identification of sarcoidosis, the detection of 14 different pulmonary diseases, the assessment of osteoarthritis severity, and the evaluation of anterior cruciate ligament (ACL) tears. This comprehensive approach ensures a thorough examination of VISION-MAE's capabilities across a broad spectrum of medical imaging challenges. We demonstrate that our model is able to achieve comparable or better performance compared to other state-of-the-art models such as nnU-Net<sup>22</sup> and TransUNet<sup>23</sup> in segmentation tasks. In classification tasks, it demonstrates similar or enhanced effectiveness when compared to methods that use supervised learning strategies, such as RadImageNet<sup>24</sup> and ImageNet<sup>25</sup> pretrained weights. Altogether, we show that the VISION-MAE SSL foundation model is able to increase performance and efficiency in a vast

array of applications, providing a versatile tool that can be applied to many different imaging modalities and anatomies.

Figure 1 provides a comprehensive overview of the development and application of VISION-MAE. During its development phase, we compiled a substantial dataset consisting of 2,486,425 images across five imaging modalities. This dataset included 1,199,904 MR images, 570,943 CT images, 657,313 PET images, 211,326 ultrasound images, and 438,521 X-ray images, all sourced from an outpatient radiology practice in New York City over the period from 2005 to 2022. Following the self-supervised learning process with these radiological images, we assessed VISION-MAE's performance and generalizability across a variety of segmentation and classification tasks. This evaluation involved 9 publicly available segmentation datasets and 5 classification datasets. Specifically, for sarcoidosis prediction using PET/MR imaging, we utilized a dataset from a separate cohort collected between 2017 and 2022 at the Mount Sinai Hospital due to the scarcity of available PET/MR datasets.

**1) Development of self-supervised foundation model RAD-SWIN-MAE**



**2) Evaluation on downstream tasks**

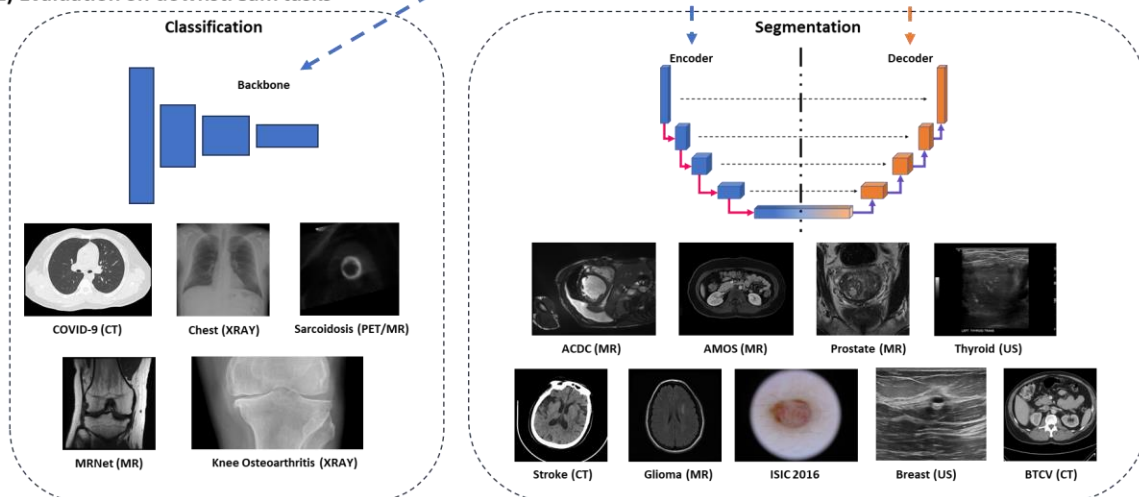


Figure 1. Overview of the study design. First, we collected a substantial upstream cohort for developing the self-supervised learning foundation model, VISION-MAE, using a masking-based SSL strategy. Second, we utilized the pretrained weights from VISION-MAE for two types of medical imaging applications: classification and segmentation. For classification tasks, the model's backbone is fine-tuned using the pretrained encoder weights from VISION-MAE. In

segmentation tasks, both the VISION-MAE's encoder and decoder weights are fine-tuned on downstream applications. This approach leverages the learned features from VISION-MAE to enhance performance in specific medical imaging tasks.

In our study, we evaluated the performance and label efficiency of VISION-MAE against two leading models in medical image segmentation, nnU-Net and TransUNet, and two supervised learning models, RadImageNet and ImageNet, for classification tasks. All these models employed distinct pretrained weights for classification but utilized the same architectural framework and fine-tuning processes for downstream applications. nnU-Net and TransUNet were configured using the default parameters recommended in their original publications. Detailed information on parameter settings can be found in the Methods section and the supplementary materials. RadImageNet is a comprehensive radiological dataset comprising 1.35 million images, annotated across 165 pathological labels and 14 anatomical regions, spanning three imaging modalities: CT, MR, and ultrasound. ImageNet, on the other hand, employs traditional transfer learning by pretraining the model through supervised learning on ImageNet-1k, which includes approximately 1.3 million natural images across 1000 categories. TransUNet also utilizes pretrained weights from ImageNet-1k. Additionally, we compared VISION-MAE with SimCLR, another popular SSL strategy within the VISION-MAE framework. SimCLR adopts a contrastive learning-based approach and maintains the same architecture and parameters for segmentation tasks as VISION-MAE. Our evaluations spanned 9 segmentation datasets and 5 classification datasets. For each dataset with less than 4000 images, we performed five-fold cross-validation. The model performances were measured using the area under the receiver operating characteristic curve (AUC) for classification tasks and the Dice Score Coefficient (DSC) for segmentation tasks. We also conducted two-sided t-tests to determine the statistical significance of the differences between VISION-MAE and each comparison model for each task.

### **VISION-MAE model on medical image segmentation**

We evaluated VISION-MAE on 9 medical image segmentation tasks of various imaging modalities and anatomies, and compared our foundation model to other benchmarks, including nnUNet, TransUNet and another SSL strategy, SimCLR. As shown in Figure 2, the VISION-MAE showed strong performance in all downstream tasks.

In the segmentation of 13 abdominal organs in the BTCV CT dataset, our VISION-MAE model showed better performance than nnUNet (DSC=0.842,  $p<0.001$ ) and SimCLR (DSC=0.820,  $p<0.001$ ) with dice score of 0.850, and achieved similar performance with TransUNet (DSC=0.854,  $p=0.309$ ). In the task of stroke segmentation, VISION-MAE outperformed self-supervised strategies nnUNet (DSC=0.696,  $p<0.05$ ) and TransUNet (0.700,  $p=0.130$ ), but underperformed against SimCLR (DSC=0.719,  $p=0.182$ ) with dice score of 0.71.

In the segmentation of 12 abdominal organs on AMOS MR dataset, our VISION-MAE model outperformed other benchmark models including nnUNet (DSC=0.877,  $p<0.001$ ), TransUNet (DSC=0.863,  $p<0.001$ ), and SimCLR (DSC=0.847,  $p<0.001$ ) with dice score of 0.891. In the segmentation of cardiac MR images on ACDC dataset, the VISION-MAE achieved a dice score

of 0.879 which was similar to nnUNet (DSC=0.883,  $p=0.057$ ) and outperformed TransUNet (DSC=0.874,  $p<0.05$ ) and SimCLR (DSC=0.861,  $p<0.001$ ). For prostate segmentation, VISION-MAE achieved dice score 0.902 and outperformed nnUNet (DSC=0.833,  $p<0.001$ ), TransUNet (DSC=0.815,  $p<0.001$ ), and SimCLR (DSC=0.802,  $p<0.001$ ). In the glioma segmentation, VISION-MAE also outperformed other benchmarks including nnUNet (DSC=0.881,  $p=0.364$ ), TransUNet (DSC=0.832,  $p<0.001$ ), and SimCLR (DSC=0.862,  $p<0.001$ ) with dice score of 0.883.

For the ultrasound breast nodule segmentation, VISION-MAE can segment breast nodules with a dice score of 0.780 which is similar to the performance of nnUNet (DSC=0.783,  $p=0.677$ ) but outperformed TransUNet (0.724,  $p<0.001$ ) and SimCLR (0.758,  $p<0.01$ ). For the ultrasound thyroid nodule segmentation, VISION-MAE outperforms all other benchmarks including nnUNet (DSC=0.716,  $p=0.164$ ), TransUNet (DSC=0.696,  $p<0.001$ ), and SimCLR (DSC=0.619,  $p<0.001$ ) with a dice score 0.720. In the ISIC 2016 dataset, VISION-MAE beat all other benchmarks including nnUNet (DSC=0.904,  $p<0.001$ ), TransUNet (DSC=0.918,  $p<0.01$ ), and SimCLR (DSC=0.910,  $p<0.001$ ) with dice score of 0.923.

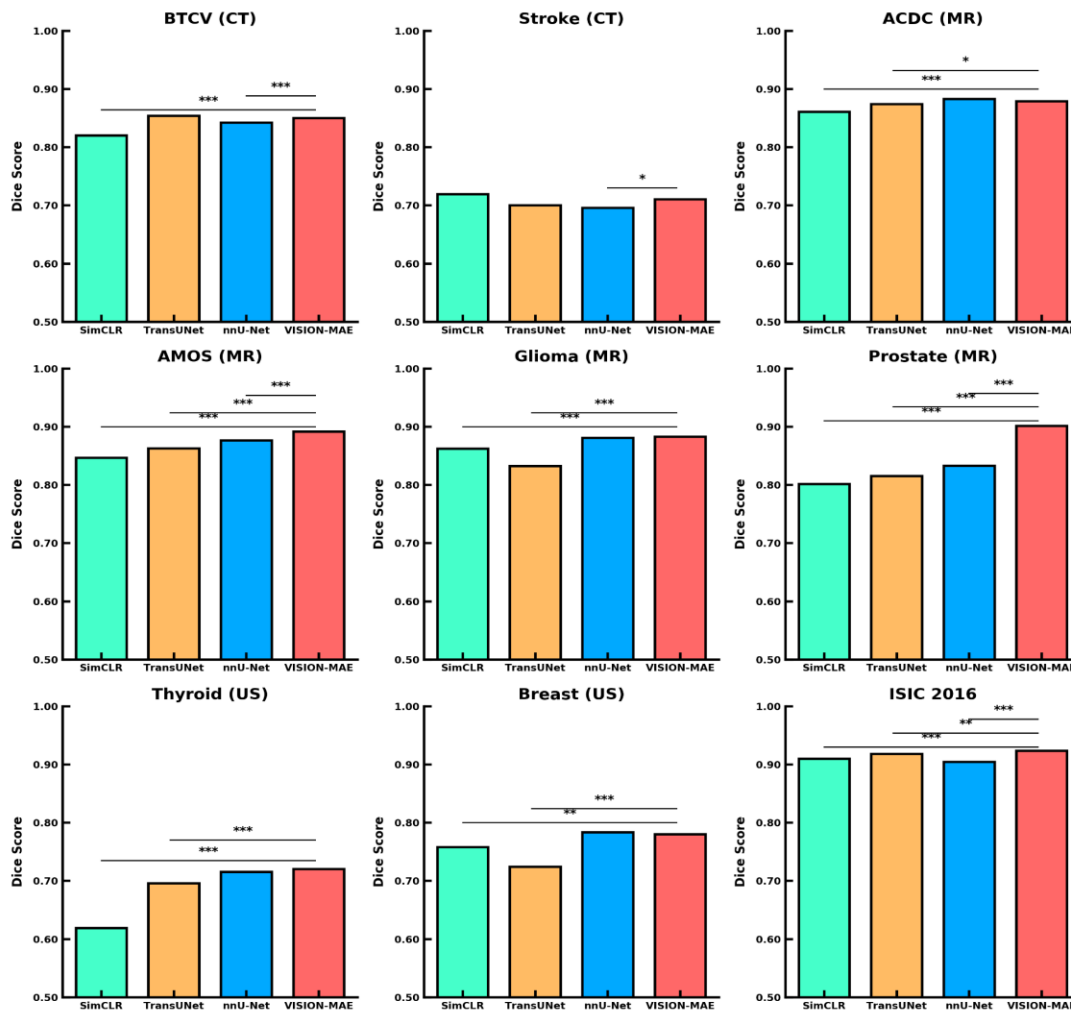


Figure 2. Performance on nine segmentation tasks in terms of dice score. VISION-MAE was finetuned and evaluated on BTCV abdomen (CT), stroke (CT), ACDC (MR), AMOS (MR), glioma (MR), prostate (MR), thyroid (US), breast (US), and ISIC 2016. Except in stroke (CT) and thyroid (US) datasets, we performed 5-fold cross validation for each dataset. Each color bar indicated the dice score of its respective model on a specific task. In each task, the dice scores between VISION-MAE and other models were compared by a two-sided t-test. The p value with statistical significance was listed as the following: \* for p value < 0.05, \*\* for p value < 0.01, and \*\*\* for p value < 0.001.

### **VISION-MAE on classification tasks**

To evaluate VISION-MAE's performance in downstream classification tasks, we included four publicly available datasets and one internal dataset. In the public datasets for COVID-19, ACL tear, Knee Osteoarthritis, and NIH Chest X-ray, VISION-MAE achieved Area Under the Curve (AUC) scores of 0.872 (0.859, 0.885), 0.946 (0.933, 0.960), 0.932 (0.923, 0.940), and 0.764 (0.760, 0.769), respectively. In our internal dataset for the classification of sarcoidosis, VISION-MAE attained an AUC of 0.665 (0.621, 0.710).

Comparatively, the self-supervised learning model SimCLR registered AUC scores of 0.848 (0.834, 0.862,  $p < 0.001$ ) for COVID-19, 0.601 (0.555, 0.647,  $p < 0.01$ ) for sarcoidosis, 0.912 (0.894, 0.929,  $p < 0.001$ ) for ACL tear, 0.894 (0.882, 0.905,  $p < 0.001$ ) for Knee Osteoarthritis, and 0.713 (0.708, 0.717) for the NIH Chest X-ray dataset.

Against supervised learning models with RadImageNet and ImageNet pretrained weights, VISION-MAE generally showed superior performance. RadImageNet achieved AUC scores of 0.867 (0.853, 0.879,  $p = 0.301$ ) for COVID-19, 0.637 (0.588, 0.685,  $p = 0.153$ ) for sarcoidosis, 0.938 (0.924, 0.951,  $p = 0.193$ ) for ACL tear, 0.903 (0.892, 0.914,  $p < 0.001$ ) for Knee Osteoarthritis, and 0.767 (0.762, 0.771) for NIH Chest X-ray. ImageNet yielded AUC scores of 0.863 (0.850, 0.875,  $p = 0.064$ ) for COVID-19, 0.616 (0.572, 0.660,  $p < 0.05$ ) for sarcoidosis, 0.937 (0.921, 0.951,  $p = 0.136$ ) for ACL tear, 0.921 (0.912, 0.930,  $p < 0.001$ ) for Knee Osteoarthritis, and 0.775 (0.770, 0.779) for NIH Chest X-ray. These results underscore VISION-MAE's efficacy, particularly in medical image classification via self-supervised learning.

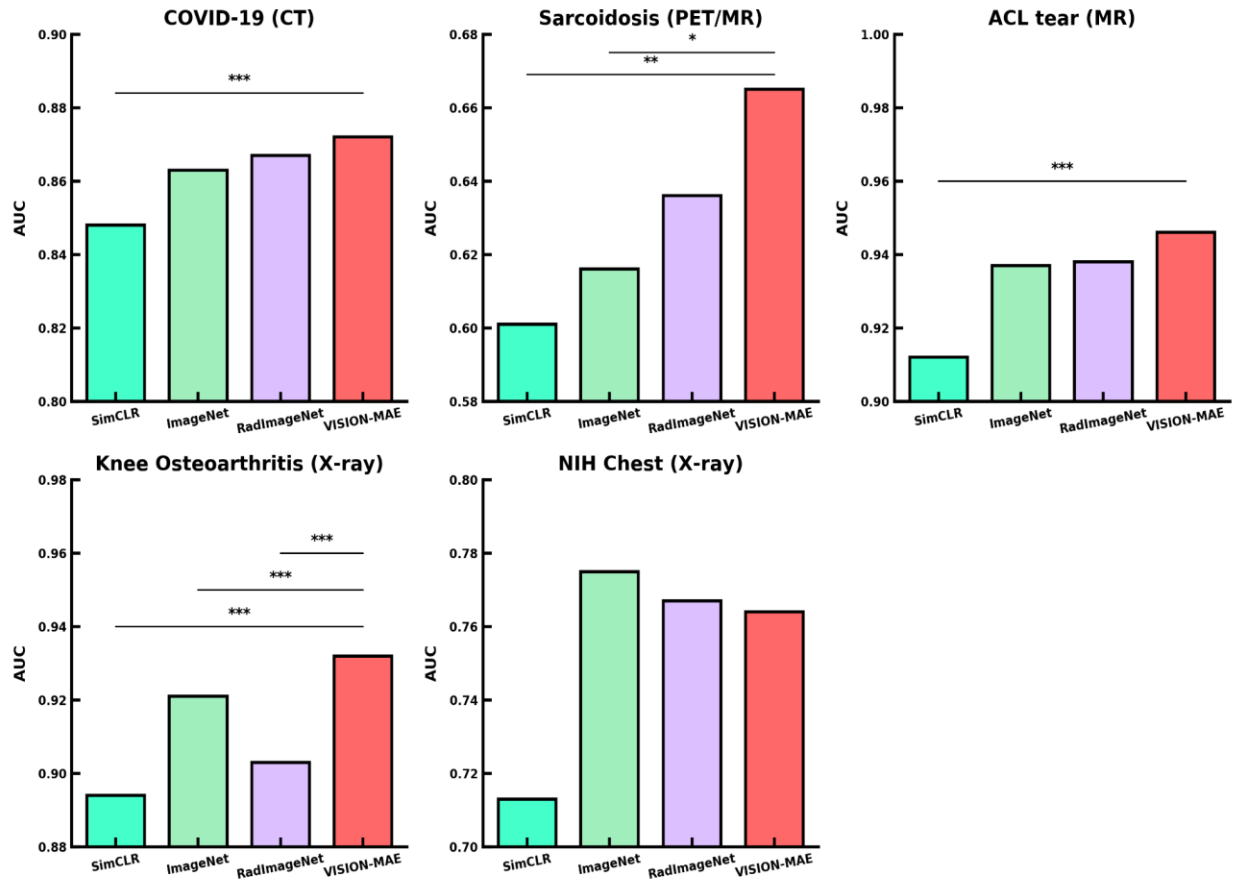


Figure 3. Performance on five classification tasks in terms of AUC score. The encoder of VISION-MAE was finetuned and evaluated on COVID-19 (CT), sarcoidosis (PET/MR), ACL tear (MR), Knee osteoarthritis (X-ray), and NIH Chest (X-ray). Except in the NIH Chest (X-ray) dataset, we performed 5-fold cross validation for each dataset. Each color bar indicated the AUC score of its respective model on a specific task. For COVID-19, sarcoidosis, ACL tear and knee osteoarthritis classification, DeLong’s test was applied to compare the AUC scores between VISION-MAE and other models. The p value with statistically significance was listed as the following: \* for p value < 0.05, \*\* for p value < 0.01, and \*\*\* for p value < 0.001.

### Label efficiency in segmentation and classification applications

Label efficiency is the measure of how much training data and annotations are needed to reach a desired level of performance in a specific task, reflecting the burden of labeling placed on medical professionals. To evaluate the label efficiency of VISION-MAE, we took a further analysis in the segmentation and classification tasks and developed models using 10%, 50%, and 80% training data. In Figure 4, we presented the results that VISION-MAE showed superior performance in various tasks compared to supervised learning strategies. In BTCV abdominal segmentation, VISION-MAE outperformed nnU-Net and SimCLR using 80% of training data. Additionally, for the AMOS dataset, VISION-MAE matched the performance of SimCLR, utilizing only 80% of training data. In the task of prostate segmentation, VISION-MAE exceeded the performance of both nnU-Net and TransUNet, achieving this with just 50% of the training data. In classification of knee osteoarthritis, VISION-MAE can achieve the performance of self-

supervised learning RadImageNet and ImageNet pretrained weight with 50% of training data. These results demonstrate the potential of VISION-MAE in alleviating data shortages in both segmentation and classification applications, leading to reduction in computational costs.

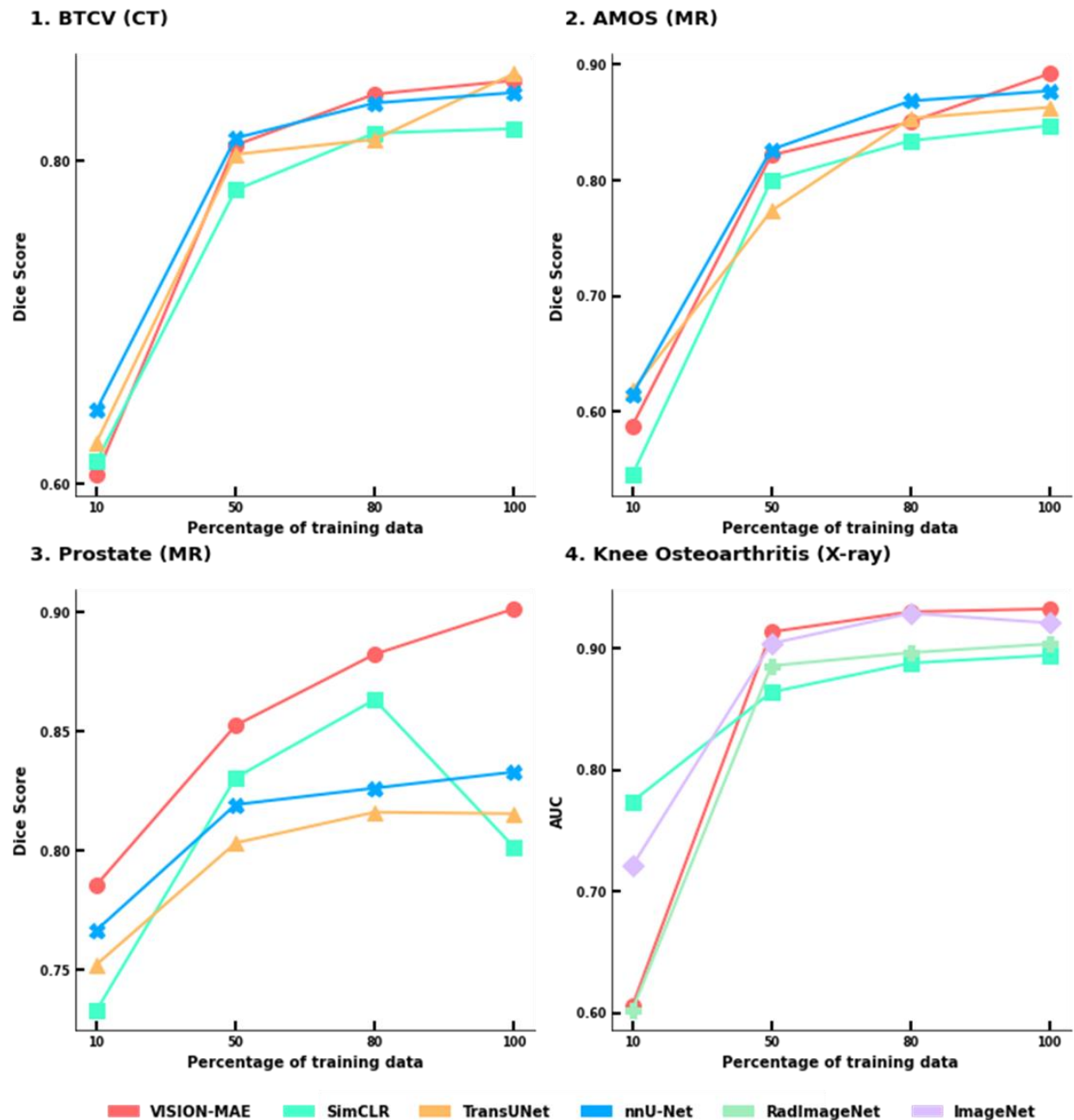


Figure 4. Label efficiency measures the performance with different percentages of training data of the six models, including VISION-MAE, SimCLR, TransUNet, nnU-Net, RadImageNet and ImageNet. All models were trained using 10%, 50%, 80% and 100% of training data in BTCV (CT), AMOS (MR), prostate (MR) segmentation datasets and the knee osteoarthritis (X-ray) classification dataset. In these downstream tasks, VISION-MAE trained with 50% training data can achieve the performances of other models with 100% training data.



## Discussion

This paper introduces VISION-MAE, a novel foundation model based on self-supervised learning (SSL), and assesses its adaptability and effectiveness in various downstream segmentation and classification tasks. Utilizing a sophisticated SSL technique, the masked autoencoder, this model is trained on a vast collection of unlabeled radiological images. This training approach enables VISION-MAE to be effectively applied to a wide array of downstream tasks, leading to substantial enhancements in segmenting different anatomical structures and lesions, as well as in classifying a variety of diseases across multiple imaging modalities. As a pioneering medical foundation model, VISION-MAE has undergone thorough development and evaluation, demonstrating significant potential for exploiting multi-modal data without the requisite for specific image-wise or pixel-wise labels.

VISION-MAE significantly enhances performance in nine segmentation tasks by employing a self-learning process that focuses on pattern recognition through image reconstruction. This model utilizes an encoder-decoder architecture (detailed in Extended Data X) to reconstruct images that have been partially masked. This process is instrumental in learning the intricate spatial patterns characteristic of medical imaging. Moreover, the architecture can be adapted into a U-Net format for segmentation, incorporating skip connections. This adaptability allows the pretrained weights of VISION-MAE's encoder and decoder to be effectively employed in segmentation tasks, which typically rely on U-Net based structures for pixel-wise predictions. This contributes to its enhanced segmentation performance when adapted to related tasks.

As illustrated in Figure 2, VISION-MAE outperforms other models in various segmentation tasks, ranking higher than nnU-Net, TransUNet, and SimCLR. nnU-Net, a benchmark model, specializes in automatic image preprocessing and configuration optimization. TransUNet, a transformer-based U-Net designed for medical imaging segmentation, leverages pretrained weights from supervised learning on ImageNet-1k, a dataset containing 1.3 million natural images across 1,000 classes. SimCLR, also pretrained on the same dataset as VISION-MAE, employs a distinct SSL technique – contrastive learning. The segmentation results demonstrate that by applying the MAE technique to unlabeled radiological images, VISION-MAE emerges as a highly generalizable model. Compared to SimCLR, VISION-MAE shows that it can learn better radiologic-specific image features and its encoder-decoder architecture performs better than SimCLR which only contains an encoder for classification during SSL pretraining. Compared to established benchmark models nnU-Net and TransUNet, VISION-MAE surpasses their performances in radiologic images but also shows better generalizability on other types of medical imaging modality, such as dermoscopy.

Due to the encoder-decoder architecture, VISION-MAE can easily adapt to downstream classification tasks by substituting the decoder with a classification layer. SSL MAE have already learned radiologic-specific image context on unlabelled data, and thus pretrained weight of VISION-MAE can be finetuned with larger learning rate and trained with less epochs in classification. For the four smaller classification tasks of COVID-19, sarcoidosis, ACL tear and knee osteoarthritis, VISION-MAE shows consistently better performance compared to supervised learning pretrained weights based on RadImageNet and ImageNet. RadImageNet is a large-scale radiologic annotated dataset of 1.35 million images across 165 pathological labels

and 14 anatomies, and it contains medical images of three modalities, CT, MR and ultrasound. While in the NIH Chest X-ray dataset, supervised learning methods performed better than VISION-MAE with no significant difference. Because this chest dataset contains over 110,000 images, it provides enough information to develop deep learning models from scratch and transfer learning becomes less effective. The classification achievements of VISION-MAE affirm the masked autoencoder's potential in establishing robust foundational models comparable to supervised learning counterparts.

Another advantage of VISION-MAE is its efficiency in label utilization for downstream applications. Constructing large datasets with high-quality annotations is particularly challenging in medical imaging because the process of medical image annotation, especially dense annotation for image segmentation, is highly resource intensive. Different from natural images, only radiology experts have the knowledge to annotate radiological images. VISION-MAE, developed through a self-supervised learning strategy on a large-scale unlabeled dataset, mitigates the time and resources needed for upstream data collection. By developing models using different portions of training data, VISION-MAE can attain optimal performances using 50% or 80% training data in BTCV, AMOS abdominal segmentation, prostate segmentation and knee osteoarthritis classification. The results on downstream applications indicate the capacity of VISION-MAE to alleviate annotation efforts in medical imaging research.

Although VISION-MAE has been systematically evaluated for its effectiveness in segmenting and predicting a variety of diseases, there are notable limitations and areas for improvement that warrant further exploration in future research. Firstly, the training process for VISION-MAE is conducted at the slice level, while CT, MR, and PET images are inherently volumetric. This approach may result in a potential oversight of the rich volumetric spatial data, which is crucial for a comprehensive understanding of medical images. Future developments could focus on incorporating volumetric data processing to fully leverage the spatial context inherent in these images. Secondly, the training cohort used in this study was sourced from an outpatient radiology practice. This selection may not adequately represent the spectrum of disease severities often observed in inpatient settings. As a result, the model might exhibit limitations in accurately recognizing and diagnosing severe diseases typically found in hospitalized patients. Future research should aim to include a more diverse dataset that encompasses both outpatient and inpatient scenarios to enhance the model's robustness and applicability across different clinical settings. Lastly, integrating multi-modal data that includes patient-specific information, such as age and sex, along with imaging protocols, could significantly enhance the fairness and reduce biases in the model. Such integration would likely improve the generalizability of VISION-MAE in downstream applications. Incorporating these additional dimensions of data can provide a more holistic view of the patient's condition, leading to more accurate and personalized diagnostic outcomes. In light of these considerations, we propose future research to focus on developing methods for processing volumetric data, expanding the training dataset to include a broader range of patient types and disease severities, and integrating multi-modal patient data to create a more comprehensive, fair, and generalizable medical imaging model. Such advancements will not only enhance the performance of VISION-MAE but also significantly contribute to the overall field of medical image analysis.

In conclusion, our evaluation of VISION-MAE demonstrates its remarkable effectiveness and adaptability across a range of downstream applications. This model exhibits superior performance and generalizability in both segmentation and classification tasks within the medical imaging domain. VISION-MAE effectively addresses the prevalent clinical challenges of requiring extensive labeled datasets and the limited generalizability of existing models. By employing self-supervised learning strategies and training on large volumes of unlabeled data, VISION-MAE marks a significant advance in medical imaging, facilitating a more efficient and precise approach that could significantly enhance diagnostic processes in healthcare.

## **Method**

### **Upstream Dataset**

The dataset we used to develop VISION-MAE, collected from a private radiology practice in New York City between 2005 and 2022, comprises 2,486,425 images including five imaging modalities: MR (1,199,904 images), CT (570,943 images), PET/CT (65,731 images), X-rays (438,521 images), and ultrasound (211,325 images). This collection builds upon our previous RadImageNet project, which contained 1.35 million images of MR, CT, and ultrasound. In this expanded dataset, we incorporated additional modalities and anatomical regions. The MR, CT, and PET/CT images were curated, focusing on those demonstrating major pathologies, selected by a reading radiologist. For X-rays and ultrasound, we included all images from each study. The dataset's age distribution is characterized by a mean value of 45 and a standard deviation of 5.

### **Downstream datasets**

For the downstream tasks, we evaluated VISION-MAE pretrained weights on 9 publicly-available segmentation datasets, including BTCV-Abdomen dataset of 2178 CT slices containing annotations of 13 abdominal organs, stroke dataset<sup>26</sup> of 4656 non-contrast-enhanced CT slices of 5 lesion labels, ACDC dataset of 2978 cardiac MR slices with annotations of left ventricle, right ventricle and epicardium, AMOS dataset of 2476 abdomen MR slices of 12 abdominal organs, prostate dataset<sup>27</sup> of 3554 MR slices of three labels, brain segmentation dataset<sup>28</sup> of 1373 MR slices with glioma abnormality mask, breast segmentation dataset<sup>29</sup> of 647 ultrasound images, thyroid segmentation dataset<sup>30</sup> of 17641 ultrasound images, and ISIC 2016 skin lesion segmentation dataset<sup>31</sup> of 1279 dermoscopic images.

In addition, we also evaluated VISION-MAE on 5 classification tasks: COVID-19 classification dataset of 9050 CT chest images, an internal sarcoidosis dataset of 1231 PET/MR cardiac images to classify sarcoidosis lesion, anterior cruciate ligament (ACL) dataset of 1021 MR knee images, knee osteoarthritis dataset of 1650 knee X-ray images with 4 labels, and NIH Chest X-ray dataset of 112,120 X-ray images of 14 pulmonary classes.

For datasets with fewer than 4,000 images, we implemented 5-fold cross-validation. In this process, the data were split into training and validation sets at a 9:1 ratio. For larger datasets, we allocated 72% of the images for training, 8% for validation, and 20% for testing. This

approach ensures robust model evaluation and generalizability across a wide spectrum of medical imaging tasks.

### **Development of VISION-MAE**

In developing VISION-MAE, we constructed a foundation model based on a Swin Transformer-driven masked autoencoder architecture, comprising both an encoder and a decoder. During preprocessing, each image from our dataset was resized and segmented into 4x4 patches, with a random selection of 75% of these patches being masked. The encoder was designed to process both masked and unmasked patches, outputting high-level feature representations. This encoder incorporated a modified version of the tiny Swin Transformer (Swin-T), consisting of four layers. Each layer was equipped with a patch merging block and two Swin Transformer blocks. The structure of each Swin Transformer block consisted of a LayerNorm (LN) layer, a multi-head self-attention module, and a residual connection followed by two MLP (multi-layer perceptron) layers. The decoder's role was to expand upon these high-level image features and reconstruct the patches to form complete images. Given that both the encoder and decoder weights were intended for fine-tuning in downstream applications using a Swin-UNet architecture, the decoder in VISION-MAE also employs Swin Transformer blocks. This enables image reconstruction through a final linear projection. The alignment of the decoder's architecture with the Swin Transformer framework is pivotal, ensuring seamless transition and compatibility when applying VISION-MAE's pretrained weights to various downstream medical imaging tasks.

### **Adaptation to downstream tasks**

In the process of adapting VISION-MAE to various downstream tasks, the selection and application of pretrained weights from its encoder and decoder were modified according to the specific requirements of each task. For the segmentation tasks involving radiological images, we finetuned both the encoder and decoder pretrained weights from VISION-MAE. For segmentation tasks dealing with color medical images, only the encoder part of VISION-MAE was utilized, while the decoder in the downstream model was initialized with random weights. When addressing classification tasks, the strategy involved leveraging the pretrained weights from the VISION-MAE encoder, complemented by the addition of a randomly initialized classification head layer.

The architectural configuration for downstream tasks diverged slightly from the upstream VISION-MAE model. Specifically, the encoder in the downstream models adhered to a Swin-T architecture with four layers, containing 2, 2, 6, and 2 Swin Transformer blocks, respectively. Notably, in the third layer of the downstream models, two blocks employed the pretrained weights from the VISION-MAE encoder, while the remaining four blocks were randomly initialized. Additionally, the decoder segment of the segmentation model incorporated skip connections, a strategic enhancement aimed at improving the accuracy and quality of the generated prediction masks. This tailored approach in the model architecture ensured that the downstream applications were optimally equipped for their specific tasks, effectively leveraging the foundational strengths of VISION-MAE while adapting to the unique demands of each application.

## **Model training**

The training regimen for the upstream VISION-MAE model was thoroughly devised, with distinct pretrained weights developed for each imaging modality: MR, CT and PET/CT, ultrasound, and X-ray. These pretrained weights were each trained using a batch size of 640 across 800 epochs. We employed the AdamW optimizer and utilized 8 NVIDIA DGX A100 GPUs for this process. The initial learning rate was set at 0.0001, and it followed a half-cycle cosine function decrement correlating with the progression of training epochs. Additionally, a preliminary warmup stage of 10 epochs was incorporated into the training process.

In the development of models for downstream segmentation tasks, we standardized the warmup period to 40 epochs, with a total of 150 training epochs. The basic learning rate and batch size were adjustable parameters, finetuned to optimize performance on the validation set before final evaluation on the test set. For the development of models in downstream classification tasks, the training encompassed 10 warmup epochs within a total of 50 training epochs, with a basic learning rate of 0.001. Here, the batch size was the only variable parameter to be fine-tuned. AdamW optimizer was consistently used across all downstream applications. Monitoring the training of segmentation models was conducted through a dual-metric approach, combining the dice coefficient and cross-entropy loss. In contrast, the training of classification models was overseen solely by cross-entropy loss.

## **Benchmark models**

To rigorously assess the performance of VISION-MAE, we conducted comparative analyses with other benchmark models in both segmentation and classification tasks. For segmentation, we developed and evaluated models using three different strategies: nnU-Net, TransUNet, and SimCLR. In the case of nnU-Net models, they were configured to mirror the data distribution of VISION-MAE and trained for an equivalent number of epochs. nnU-Net distinguished itself with its unique pre-processing method for managing its training process. The TransUNet models, on the other hand, were trained using the default stochastic gradient descent (SGD) optimizer with a learning rate of 0.01, over the training of 150 epochs. The SimCLR pretrained weights were developed with the same upstream data as VISION-MAE using Swin Transformer architecture using SimCLR self-supervised learning strategy. Then, the SimCLR pretrained models were aligned with VISION-MAE in terms of training parameters for downstream tasks, ensuring a fair and consistent comparison.

For classification tasks, VISION-MAE was benchmarked against models that used supervised learning Swin Transformer pretrained weights, specifically those trained on RadImageNet and ImageNet datasets, and the self-supervised learning SimCLR. These pretrained models were fine-tuned using the same parameters as those applied to VISION-MAE in downstream tasks.

## **Statistics**

For segmentation tasks, we employed the dice score as the primary evaluation metric. To establish the reliability of the dice score results, we calculated the 95% confidence interval (CI) using a bootstrapping method involving 1,000 resamples. For statistical analysis in segmentation tasks, we utilized the paired t-test to identify the most competitive model, ensuring that the differences in performance were not only apparent but also statistically significant.

Classification tasks were evaluated using the Area Under the Receiver Operating Characteristic curve (AUROC). In the realm of binary classification, we employed DeLong's test to ascertain both the 95% confidence interval and the statistical significance of performance differences between various models on individual labels. For more complex scenarios involving multi-class and multi-label classifications, we again used bootstrapping with 1,000 resamples. This method was used to calculate the 95% confidence interval and to determine the p-value between different models.

## References

1. Bommasani, R. *et al.* On the Opportunities and Risks of Foundation Models. Preprint at <https://doi.org/10.48550/arXiv.2108.07258> (2022).
2. Mei, X., Liu, Z., Singh, A. *et al.* Interstitial lung disease diagnosis and prognosis using an AI system integrating longitudinal data. *Nat Commun* 14, 2272 (2023).
3. Mei, X., Lee, HC., Diao, Ky. *et al.* Artificial intelligence-enabled rapid diagnosis of patients with COVID-19. *Nat Med* 26, 1224–1228 (2020).
4. Zech, J. R. *et al.* Variable generalization performance of a deep learning model to detect pneumonia in chest radiographs: A cross-sectional study. *PLOS Medicine* 15, e1002683 (2018).
5. Kirillov, A. *et al.* Segment Anything. Preprint at <https://doi.org/10.48550/arXiv.2304.02643> (2023).
6. Ma, J., He, Y., Li, F. *et al.* Segment anything in medical images. *Nat Commun* 15, 654 (2024). <https://doi.org/10.1038/s41467-024-44824-z>
7. Nguyen, D. M. H. *et al.* LVM-Med: Learning Large-Scale Self-Supervised Vision Models for Medical Imaging via Second-order Graph Matching. Preprint at <https://doi.org/10.48550/arXiv.2306.11925> (2023).
8. Yan, Z. *et al.* A Foundation Model for General Moving Object Segmentation in Medical Images. Preprint at <https://doi.org/10.48550/arXiv.2309.17264> (2023).
9. Du, Y., Bai, F., Huang, T. & Zhao, B. SegVol: Universal and Interactive Volumetric Medical Image Segmentation. Preprint at <https://doi.org/10.48550/arXiv.2311.13385> (2023).
10. Zhou, Y., Chia, M.A., Wagner, S.K. *et al.* A foundation model for generalizable disease detection from retinal images. *Nature* 622, 156–163 (2023). <https://doi.org/10.1038/s41586-023-06555-x>
11. Qiu, J. *et al.* VisionFM: a Multi-Modal Multi-Task Vision Foundation Model for Generalist Ophthalmic Artificial Intelligence. Preprint at <https://doi.org/10.48550/arXiv.2310.04992> (2023).
12. Campanella, G. *et al.* Computational Pathology at Health System Scale -- Self-Supervised Foundation Models from Three Billion Images. Preprint at <https://doi.org/10.48550/arXiv.2310.07033> (2023).
13. Chen, X. *et al.* Recent advances and clinical applications of deep learning in medical image analysis. *Med Image Anal* 79, 102444 (2022).
14. Soffer, S. *et al.* Convolutional Neural Networks for Radiologic Images: A Radiologist's Guide. *Radiology* 290, 590–606 (2019).

15. Langlotz, C. P. *et al.* A Roadmap for Foundational Research on Artificial Intelligence in Medical Imaging: From the 2018 NIH/RSNA/ACR/The Academy Workshop. *Radiology* **291**, 781–791 (2019).
16. Li, J. *et al.* A Systematic Collection of Medical Image Datasets for Deep Learning. Preprint at <https://doi.org/10.48550/arXiv.2106.12864> (2021).
17. Willeminck, M. J. *et al.* Preparing Medical Imaging Data for Machine Learning. *Radiology* **295**, 4–15 (2020).
18. Park, S. H. & Han, K. Methodologic Guide for Evaluating Clinical Performance and Effect of Artificial Intelligence Technology for Medical Diagnosis and Prediction. *Radiology* **286**, 800–809 (2018).
19. Chen, T., Kornblith, S., Norouzi, M. & Hinton, G. A Simple Framework for Contrastive Learning of Visual Representations. *Proceedings of the 37th International Conference on Machine Learning* 1597–1607 (2020).
20. He, K. *et al.* Masked Autoencoders Are Scalable Vision Learners. *Proceedings - 2022 IEEE/CVF Conference on Computer Vision and Pattern Recognition, CVPR 2022* 15979–15988 (2022) doi:10.1109/CVPR52688.2022.01553.
21. Xu, Z. *et al.* Swin MAE: Masked autoencoders for small datasets. *Comput Biol Med* **161**, 107037 (2023).
22. Isensee, F., Jaeger, P. F., Kohl, S. A. A., Petersen, J. & Maier-Hein, K. H. nnU-Net: a self-configuring method for deep learning-based biomedical image segmentation. *Nat Methods* **18**, 203–211 (2021).
23. Chen, J. *et al.* TransUNet: Transformers Make Strong Encoders for Medical Image Segmentation. Preprint at <https://doi.org/10.48550/arXiv.2102.04306> (2021).
24. Mei, X. *et al.* RadImageNet: An Open Radiologic Deep Learning Research Dataset for Effective Transfer Learning. *Radiology: Artificial Intelligence* **4**, e210315 (2022).
25. Deng, J. *et al.* ImageNet: A large-scale hierarchical image database. in *2009 IEEE Conference on Computer Vision and Pattern Recognition* 248–255 (2009). doi:10.1109/CVPR.2009.5206848.
26. Liang, K. *et al.* Symmetry-enhanced attention network for acute ischemic infarct segmentation with non-contrast CT images. *Medical Image Computing and Computer Assisted Intervention – MICCAI 2021* 432–441 (2021). doi:10.1007/978-3-030-87234-2\_41
27. Adams, L. C. *et al.* Prostate158 - An expert-annotated 3T MRI dataset and algorithm for prostate cancer detection. *Computers in Biology and Medicine* **148**, 105817 (2022).



28. Buda, M., Saha, A. & Mazurowski, M. A. Association of genomic subtypes of lower-grade gliomas with shape features automatically extracted by a deep learning algorithm. *Computers in Biology and Medicine* **109**, 218–225 (2019).
29. Al-Dhabyani, W., Gomaa, M., Khaled, H. & Fahmy, A. Dataset of breast ultrasound images. *Data in Brief* **28**, 104863 (2020).
30. Thyroid Ultrasound Cine-clip. *Stanford AIMI Shared Datasets*, (2021).  
<https://stanfordaimi.azurewebsites.net/datasets/a72f2b02-7b53-4c5d-963c-d7253220bfd5>.
31. Gutman, D. *et al.* Skin Lesion Analysis toward Melanoma Detection: A Challenge at the International Symposium on Biomedical Imaging (ISBI) 2016, hosted by the International Skin Imaging Collaboration (ISIC). Preprint at <https://doi.org/10.48550/arXiv.1605.01397> (2016).